Impaired inhibitory GABAergic synaptic transmission and transcription studied in single neurons by Patch-seq in Huntington's disease

Foteini Paraskevopoulou[a,b], Poorya Parvizi[c,1], Gökçe Senger[c,2], Nurcan Tuncbag[c,d,e], Christian Rosenmund[a,b,3], and Ferah Yildirim[b,f,3]

[a]Department of Neurophysiology, Charité–Universitätsmedizin Berlin, 10117 Berlin, Germany; [b]NeuroCure Cluster of Excellence, Charité–Universitätsmedizin Berlin, 10117 Berlin, Germany; [c]Graduate School of Informatics, Department of Health Informatics, Middle East Technical University, 06500 Ankara, Turkey; [d]Department of Chemical and Biological Engineering, College of Engineering, Koc University, 34450 Istanbul, Turkey; [e]School of Medicine, Koc University, 34450 Istanbul, Turkey; and [f]Department of Neuropsychiatry, Department of Psychiatry and Psychotherapy, Charité–Universitätsmedizin Berlin, 10117 Berlin, Germany

Edited by Anders Björklund, Lund University, Lund, Sweden, and approved March 19, 2021 (received for review September 28, 2020)

Transcriptional dysregulation in Huntington's disease (HD) causes functional deficits in striatal neurons. Here, we performed Patch-sequencing (Patch-seq) in an in vitro HD model to investigate the effects of mutant Huntingtin (Htt) on synaptic transmission and gene transcription in single striatal neurons. We found that expression of mutant *Htt* decreased the synaptic output of striatal neurons in a cell autonomous fashion and identified a number of genes whose dysregulation was correlated with physiological deficiencies in mutant Htt neurons. In support of a pivotal role for epigenetic mechanisms in HD pathophysiology, we found that inhibiting histone deacetylase 1/3 activities rectified several functional and morphological deficits and alleviated the aberrant transcriptional profiles in mutant Htt neurons. With this study, we demonstrate that Patch-seq technology can be applied both to better understand molecular mechanisms underlying a complex neurological disease at the single-cell level and to provide a platform for screening for therapeutics for the disease.

Huntington's disease | single-cell RNA sequencing | Patch-seq | synaptic function | striatum

Huntington's disease (HD) is an autosomal dominant neurodegenerative disorder characterized by progressive motor, cognitive, and psychiatric symptoms (1). Neuronal degeneration primarily occurs in GABAergic medium spiny neurons (MSN), which account for more than 90% of the neurons in striatum (2, 3). As the pathology progresses, brain regions in addition to striatum, and in particular the cortex, are affected (4). While the genetic basis of HD is known—it is caused by an expansion of polyglutamine repeats (polyQ) in exon 1 of the huntingtin (*HTT*) gene (5)—the molecular mechanisms underlying neuronal dysfunction are not fully understood.

Postmortem neuropathological studies provide little evidence for neuron loss in brain during early stages, despite clinical manifestation of HD, suggesting that neuronal dysfunction rather than neuronal death underlies early pathological manifestations of *HTT* mutation in patients (6). In accordance with this, well-established animal models recapitulate many of the molecular, neuropathological, and phenotypic disease features without apparent neuronal death, especially during early stages (7). In fact, miscommunication between neurons, commonly related to cellular morphological changes and synaptic dysfunction, has been shown to cause most HD symptoms (8, 9). Studies in transgenic mouse models and in postmortem HD patient brains revealed distinct morphological abnormalities in MSN dendrites (10), including a decrease in number of spines and an increase in shaft diameter (11). While such structural changes in MSN morphology will likely influence striatal physiology, mutant Htt has also been suggested to directly affect neurotransmitter release, either by influencing protein–protein interactions (12, 13) and vesicular trafficking (14) or by changing the gene expression of striatal neurons (15, 16).

Previous research on HD pathogenesis has shown that abnormal translocation of mutant Htt into the nucleus alters its interaction with transcription factors and regulators of gene expression, leading to changes in messenger RNA (mRNA) levels (17). Transcriptomic analyses revealed that genes related to neurotransmission as well as the establishment of MSN identity and function (i.e., *Darpp32*, *Penk*, *Drd1*, or *Drd2*) are down-regulated in the striatum of HD animal models and in caudate nucleus of patients, while stress-related genes are up-regulated (18–21). However, which mechanisms are relevant for transcriptional dysregulation in HD and how these changes affect neuronal function require further investigation.

In this study, we adapted a culture system (autapses; ref. 22) to effectively model the impact of a rapid introduction of the expression of a significantly expanded repeat length CAG into a neuron and identify neuron-specific functional changes. A healthy genetically normal neuron was efficiently exposed to the expression of an

Significance

Although the genetic basis of HD is known, the molecular mechanisms underlying neuronal dysfunction remain unclear. Combining electrophysiological and transcriptional analyses of single neurons (Patch-sequencing [Patch-seq]), this study connects transcriptional dysregulation and synaptic transmission deficits, two key disease features, in HD. We identify a number of genes whose expression changes are correlated with physiological deficiencies in mutant Htt neurons. We validate the use of the Patch-seq system for screening and identifying potential therapeutic interventions. We show that pharmacological inhibition of an epigenetic regulator rectifies several functional, morphological, and transcriptional deficits in mutant neurons. This work suggests previously unknown gene–neuronal function relationships as potential targets in HD and also highlights advances in single-cell transcriptomics and their use in understanding human disease.

Author contributions: F.P., C.R., and F.Y. designed research; F.P. performed all experiments; F.P., P.P., G.S., and N.T. analyzed and visualized the data; F.P., P.P., G.S., N.T., C.R., and F.Y. interpreted the data; F.P. wrote the paper with contributions from F.Y. regarding the RNA-seq results; and all authors edited versions of the manuscript.

The authors declare no competing interest.

This article is a PNAS Direct Submission.

[1]Present address: Usher Institute, The University of Edinburgh, EH16 4UX Edinburgh, United Kingdom.

[2]Present address: Department of Experimental Oncology, European Institute of Oncology, 20139 Milan, Italy.

[3]To whom correspondence may be addressed. Email: christian.rosenmund@charite.de or ferah.yildirim@charite.de.

This article contains supporting information online at https://www.pnas.org/lookup/suppl/doi:10.1073/pnas.2020293118/-/DCSupplemental.

Published May 5, 2021.

Htt polypeptide containing a longer-expanded CAG repeat (97Q-Htt) using a lentiviral gene transfer system. We then assessed the synaptic function and transcriptional profile of the individual neurons in the resulting cell population by combining whole-cell patch clamp measurements with single-cell RNA sequencing (Patch-sequencing [Patch-seq]; ref. 23). We quantified a number of physiological and morphological traits of striatal GABAergic neurons expressing the wild-type (25Q-Htt) or mutant (97Q-Htt) *Htt*. We found that introducing 97Q-Htt construct into neurons rapidly leads to a cell autonomous alteration in synaptic transmission and a change in transcriptional output of the neuron which is likely causative for the altered synaptic function. Furthermore, we evaluated the extent to which our Patch-seq–based system could be useful for the screening and identification of therapeutic interventions which may be useful in reversing or preventing HD symptomology and pathology. For this purpose, we evaluated the molecule RGFP109, a specific HDAC1/3 (class I) inhibitor in the Patch-seq system. Our rationale for this choice is a strong history in which epigenetic alterations are implicated in transcriptional dysregulation in HD (reviewed in ref. 24) particularly through changes in acetylation of histone proteins. We found that HDAC inhibitor (HDACi) treatment with RGFP109 partially alleviated the transcriptional changes and reverted several functional and morphological phenotypes measured in mutant 97Q-Htt neurons, suggesting a potential beneficial effect of RGFP109 in HD. The extension of this approach to a high throughput screening protocol should allow a broader and more comprehensive screening strategy for small molecules that may be effective in HD therapy.

Results

Expression of Mutant Huntingtin Decreases the Magnitude of Inhibitory Evoked Synaptic Responses in Mouse Autaptic Striatal Neurons. In order to identify the effects of mutant huntingtin on the regulation of GABAergic synaptic transmission, at single-cell level, we created an in vitro HD model using the autaptic culture system (22). Isolated striatal neurons from newborn C57BL6 mice were infected with lentiviruses expressing human *HTT* exon 1 fused to green fluorescent protein (GFP) with normal (25Q-Htt) or expanded (97Q-Htt) number of glutamine (Q) repeats (Fig. 1 *A* and *B*). Neurons expressing 25Q-Htt exhibited diffuse GFP labeling (Fig. 1 *A*, *Left*), whereas neurons expressing the mutant 97Q-Htt accumulated the protein in the nucleus and formed Htt inclusions (Fig. 1 *A*, *Right*). Neurons expressing only GFP reporter under synapsin promoter were used as control. qRT-PCR revealed that expression of 97Q-Htt leads to transcriptional dysregulation of well-known HD-related genes (i.e., *Adora2a*, *Bdnf*, *Drd1*, *Drd2*, *Ppp1r1b*, and *Polr2a*; *SI Appendix*, Fig. S1) in both striatal and cortical mass cultures, suggesting that our in vitro model can recapitulate important aspects of HD pathogenesis.

Using whole-cell patch clamp of striatal autaptic neurons, we next investigated the effects of mutant Htt on GABAergic synaptic transmission. Action potential–evoked inhibitory postsynaptic currents (IPSCs) in neurons expressing mutant 97Q-Htt were reduced by 63% compared with respective neurons expressing wild-type 25Q-Htt (Fig. 1 *C* and *D*; 11.4 ± 1.2 nA; $n = 59$ for 25Q-Htt, 4.2 ± 0.6 nA; $n = 55$ for 97Q-Htt). In addition, the synaptic response was reduced by 54% compared with control neurons expressing only GFP reporter, verifying that expression of wild-type *Htt* exon 1 in 25Q-Htt neurons did not cause a gain-of-function phenotype (9.1 ± 1.0 nA; $n = 56$ for empty vector). Furthermore, 97Q-Htt neurons showed 27% smaller membrane capacitance (C_m) compared with 25Q-Htt neurons (Fig. 1*E*; 20.3 ± 1.4 pF; $n = 59$ for 25Q-Htt versus 14.8 ± 0.8 pF; $n = 55$ for 97Q-Htt), an indication of a decrease in cell surface area, which may contribute to impairment of synaptic function.

Expression of Mutant Huntingtin Impairs Synaptic Transmission by Altering both the Quantal Size and the Number of Readily Releasable Vesicles. The magnitude of the evoked response is determined by the postsynaptic response to the release of an individual vesicle (quantal size), the number of fusion competent vesicles (readily releasable pool, RRP), and the probability that a fusion-competent vesicle is released in response to an action potential (vesicular release probability, P_{vr}) (25, 26).

To assess the parameters that underlie the observed decrease in evoked IPSC of striatal neurons, we first evaluated the spontaneous release activity. We found a 22% decrease in the mean miniature IPSC (mIPSC) amplitude of 97Q-Htt neurons (58.0 ± 3.4 pA; $n = 55$) compared with 25Q-Htt neurons (74.0 ± 3.4 pA; $n = 68$) (Fig. 1 *F* and *G*) and a 25% decrease in mIPSC charge (1327 ± 74 fC; $n = 49$ for 25Q-Htt, 1001 ± 56 fC; $n = 39$ for 97Q-Htt; $P = 0.0019$). This suggests that IPSC reduction is partially caused by a reduction in quantal size. In addition, we found that the mIPSC frequency was reduced by 44% in 97Q-Htt neurons (Fig. 1*H*; 1.1 ± 0.2 Hz; $n = 50$ for 25Q-Htt versus 0.6 ± 1.2 Hz; $n = 42$ for 97Q-Htt). As the spontaneous release frequency may reflect various properties, such as synapse number or RRP, we went on to examine more synaptic parameters in detail.

To measure the number of vesicles readily available for release (RRP size), we applied a hypertonic solution, which forces fusion of all fusion-competent vesicles (27). We quantified the RRP by integrating the transient component of the inward current, which showed a 54% decrease in 97Q-Htt (2.0 ± 0.3 nC; $n = 50$) compared with 25Q-Htt (4.3 ± 0.5 nC; $n = 50$) neurons (Fig. 1 *I* and *J*). In addition, we computed the total number of vesicles in the RRP by dividing the total RRP charge by the average charge of the miniature events from each neuron. We found that the mean number of synaptic vesicles contained in the RRP of neurons expressing 97Q-Htt (2,124 ± 360 vesicles; 38) was 38% smaller than the number in neurons expressing 25Q-Htt (3,443 ± 398 vesicles; 41) (Fig. 1*K*).

To assess whether mutant Htt also affects the efficiency of synaptic release, we computed the presynaptic P_{vr}, by dividing the evoked response charge by the RRP charge from the same neuron. We found no significant changes in P_{vr} between 25Q- and 97Q-Htt–expressing neurons (15.3 ± 1.2%; 50 for 25Q-Htt, 12.1 ± 1.0%; 46 for 97Q-Htt; $P = 0.066$) (Fig. 1*N*). Consistent with no change in P_{vr}, we observed no differences in paired-pulse ratio (0.7 ± 0.05; 50 for 25Q-Htt versus 0.8 ± 0.05; 46 for 97Q-Htt; $P = 0.34$) (Fig. 1 *L* and *M*), suggesting that 97Q-Htt alters RRP size without affecting the probability of action potential–evoked vesicle fusion (P_{vr}).

In general, expression of 25Q-Htt in neurons had no impact on spontaneous release, RRP size, or short-term plasticity compared with control neurons expressing only GFP, confirming again that overexpression of wild-type *Htt* exon 1 in neurons was not associated with gain- or loss-of-function effects.

Mutant Huntingtin Reduces Synapse Number Consistent with a Decrease in the RRP. As we observed both a decreased membrane capacitance, indicative of a decreased surface area, and a reduced RRP, indicative of reduced synapse formation, in 97Q-Htt neurons (Fig. 1), we hypothesized that mutant Htt impairs cell growth. To provide more evidence for impaired cell growth, we performed immunocytochemistry on single striatal neurons labeled with VGAT and MAP2 antibodies to mark for synapses and soma/dendrites, respectively (Fig. 2*A*). We traced the soma and dendritic trees of GFP-positive neurons (Fig. 2*A*) and found that the soma area was 15% smaller in 97Q-Htt striatal neurons (128 ± 7 μm^2; 42 for 25Q-Htt versus 109 ± 4 μm^2; 42 for 97Q-Htt) (Fig. 2*B*), consistent with the change in membrane capacitance (Fig. 1*E*). In addition, we found a 31% reduction in the number of VGAT puncta per 97Q-Htt neuron (224 ± 20; 43 for 25Q-Htt versus 180 ± 14; 44 for 97Q-Htt) (Fig. 2*C*), a change in close accordance with the decrease in the number of RRP vesicles revealed by our electrophysiology analysis (Fig. 1 *I–K*). Furthermore, we measured the total dendritic length to examine whether the decrease in synapse number was a result of a smaller dendritic arbor, but we found no significant change in total dendritic length dependent on which form of Htt was expressed

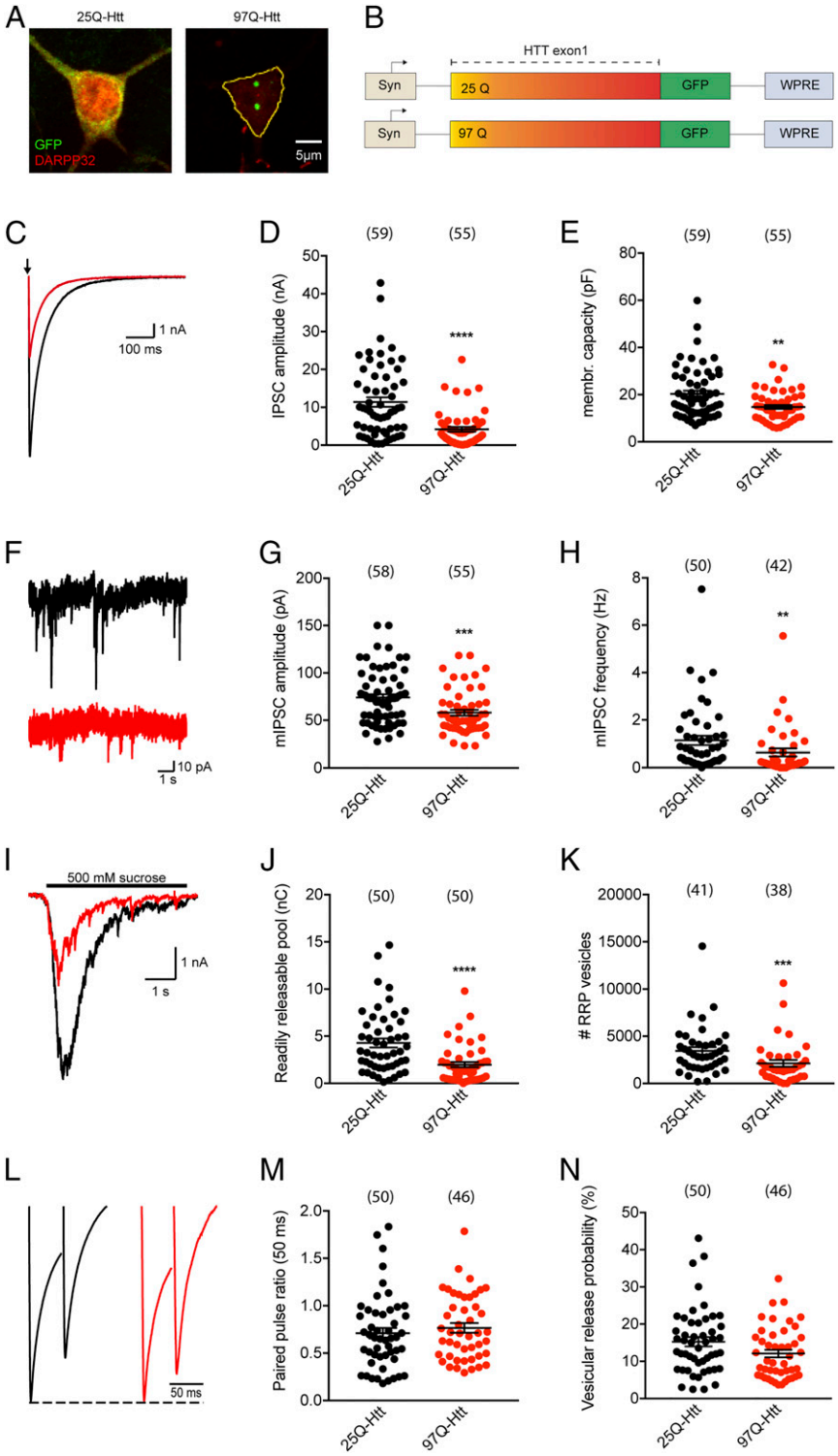

Fig. 1. Expression of mutant huntingtin (97Q-Htt) decreases synaptic transmission in autaptic striatal GABAergic neurons. (*A*) Representative images from cultured striatal neurons expressing 25Q-Htt (*Left*) and 97Q-Htt (*Right*) with immunoreactivity against GFP fusion protein (green) and the striatal neuron marker DARPP32 (red). (*B*) Schematic representation of lentiviral constructs used for infecting striatal neurons from C57BL/6N mouse. GFP sequence is fused to exon 1 of wild-type (25Q) or mutant (97Q) HTT gene. (*C–N*) Functional analysis of 25Q-Htt (black traces and bars) or 97Q-Htt (red traces and bars) neurons. (*C*) Representative traces of evoked IPSCs. (*D* and *E*) Bar graphs showing mean evoked IPSC amplitudes (*D*) and mean membrane capacitance measurements as obtained from the membrane test pulse (*E*). (*F*) Representative traces showing mIPSC activity. (*G* and *H*) Bar graphs showing mean mIPSC amplitudes (*G*) and frequency (*H*). (*I*) Representative current traces of the response to a 5 s pulse of 500 mOsm hypertonic sucrose solution. (*J* and *K*) Bar graphs showing RRP size as measured by the charge of the transient response component (*J*) and the mean number of synaptic vesicles contained in the RRP (*K*). (*L*) Representative traces of the response to paired pulse, in which both traces are normalized to the first peak of 25Q-Htt neurons (dotted line). (*M* and *N*) Bar graphs showing mean paired pulse ratios (*M*) and mean vesicular probability (P_{vr}) (*N*). Data shown as mean ± SEM. Numbers in parentheses indicate sample sizes. Mann–Whitney *U* test: * refers to $P \leq 0.05$, ** $P \leq 0.01$, *** $P \leq 0.001$, and **** $P \leq 0.001$.

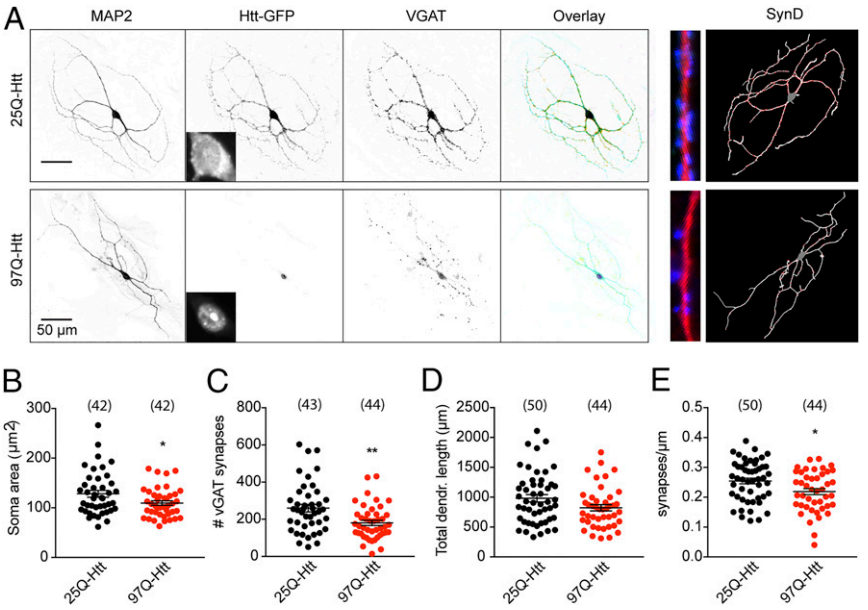

Fig. 2. Mutant huntingtin impairs cell outgrowth in autaptic striatal GABAergic neurons. (*A*) Representative images from 25Q-Htt and 97Q-Htt striatal autaptic neurons in culture showing immunoreactivity for MAP2, Htt-GFP, and VGAT and tracing of the same neurons with SynD. (*B–E*) Morphological analysis of 25Q-Htt (black bars) or 97Q-Htt (red bars) neurons. Bar graphs showing soma area (*B*), number of VGAT puncta per neuron (*C*), total length of dendrites (*D*), and the number of VGAT puncta per µm of dendritic length (*E*). Data shown as mean ± SEM. Numbers in parentheses indicate sample sizes. Mann–Whitney *U* test: * refers to $P \leq 0.05$ and ** $P \leq 0.01$.

(981 ± 61 µm; 50 for 25Q-Htt versus 822 ± 51 µm; 44 for 97Q-Htt) (Fig. 2*D*). Finally, we calculated the synapse density by dividing the number of dendritic synapses by the total dendritic length. As expected, there was a significant decrease in synapse density in 97Q-Htt neurons (0.25 ± 0.01 syn/µm; 50 for 25Q-Htt versus 0.20 ± 0.01 syn/µm; 44 for 97Q-Htt) (Fig. 2*E*), suggesting that the driving force behind the decrease in the number of vesicles in the RRP in 97Q-Htt neurons is most likely the decrease of the number of synaptic connections.

HDACi RGFP109 Restores Evoked IPSC Amplitude, RRP Size, Synapse Number, and Soma Size in Striatal Neurons Expressing Mutant Huntingtin. Transcriptional dysregulation is a major molecular feature in HD pathophysiology, and its basis appears to be the aberrant protein–protein interactions of mutant Htt with a variety of transcription factors. In our study, we tested whether targeting altered transcription through HDAC inhibition would rectify the functional and morphological phenotypes of our HD in vitro model. For this aim, we treated cultured striatal neurons with RGFP109, a specific HDAC1/3 inhibitor (100 nM treatments at days in vitro (DIV) 6, 9, and 12). For all parameters, we compared RGFP109-treated 97Q-Htt neurons with 1) vehicle-treated 25Q-Htt, 2) vehicle-treated neurons expressing only GFP (control; empty vector), and 3) with untreated 97Q-Htt neurons.

Indeed, in 97Q-Htt neurons, RGFP109 treatment resulted in a 52% increase in evoked IPSC amplitude (4.8 ± 0.6 nA; 73 for 97Q-Htt versus 8.4 ± 1.1 nA; 74 for 97Q-Htt+RGFP109) and a 38% increase in RRP charge, as compared with untreated 97Q-Htt neurons (Fig. 3 *A* and *B*; 1.8 ± 0.2 nC; 72 for 97Q-Htt versus 2.8 ± 0.3 nC; 68 for 97Q-Htt+RGFP109). The drug treatment did not significantly affect the amplitude or frequency of spontaneous events (Fig. 3*C*), paired-pulse behavior, or vesicular release probability (Fig. 3*F*) in either 25Q-Htt or 97Q-Htt neurons. While application of RGFP109 in 25Q-Htt neurons showed a trend toward decreased evoked response and RRP size, the change was not significant compared with 25Q-Htt–untreated neurons (Fig. 3 *B*, *D*, and *E*).

To assess morphological changes, we analyzed cell size, synapse number, and dendrite length from single control, 25Q-Htt, and 97Q-Htt neurons treated with vehicle or RGFP109 (Fig. 4*A*). When 97Q-Htt neurons were treated with RGFP109, soma size and synapse number in 97Q-Htt neurons were rescued by 17% (94 ± 3 µm^2; 89 for 97Q-Htt versus 114 ± 4 µm^2; 84 for 97Q-Htt+RGFP109) and 37% (125 ± 10 vesicles; 90 for 97Q-Htt versus 197 ± 13 vesicles; 85 for 97Q-Htt+RGFP109), respectively (Fig. 4 *B*, *C*, and *E*), even though dendritic length remained unaffected (Fig. 4*D*). The soma size, number of VGAT-positive puncta per neuron, and the total dendritic length of 25Q-Htt neurons were also indistinguishable from control neurons (Fig. 4; dotted line), confirming again no gain- or loss-of-function effect due to expression of wild-type *Htt* exon 1.

Additionally, we examined the effect of RGFP109 on an MSN marker protein for dopamine signaling, DARPP32. We found that 97Q-Htt neurons displayed a significant reduction in DARPP32 intensity compared with both 25Q-Htt (54%) and control neurons (61%), which was then partially reversed upon RGFP109 application by 36% ($P = 0.21$, $P = 0.22$ for 25Q-Htt versus 97Q-Htt+RGFP109) (Fig. 4*F*).

Collectively, these results illustrate the alteration of epigenetic transcriptional regulation as a pathophysiological mechanism for synaptic transmission deficits induced by mutant *Htt* expression in striatal neurons and promote a potential therapeutic role of selective HDAC1/3 inhibition in HD.

Single-Cell Transcriptome Analysis of Striatal Neurons Characterized by Electrophysiology. To examine the relationship between gene expression and the physiological properties of striatal neurons expressing mutant *Htt*, we generated single-cell transcriptome data from the same neurons that were analyzed for electrophysiology by using Patch-seq (*SI Appendix*, Fig. S2).

After recording, the soma and nucleus of neurons was extracted by the patch pipet (*SI Appendix*, Fig. S2*A*). From the harvested cell contents, poly-A–selected mRNA was converted to complementary DNA (cDNA) and used to generate single-cell RNA sequencing (RNA-seq) libraries following the Smart-seq v4 protocol (23) (*SI Appendix*, Fig. S2*B*). Libraries with low cDNA quantity and quality were excluded from sequencing. In total, we sequenced

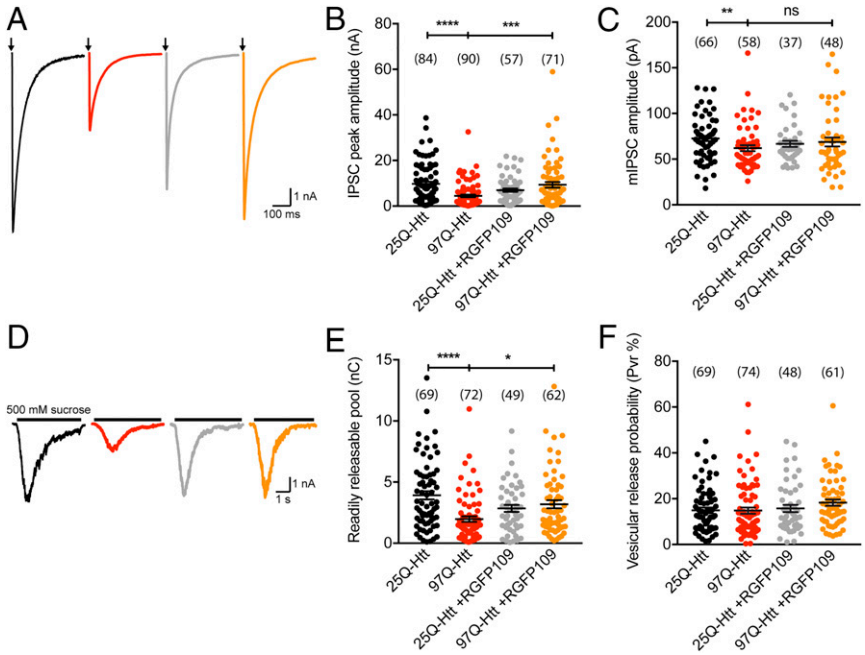

Fig. 3. Application of HDACi RGFP109 restores evoked IPSC magnitude and RRP size. (*A*–*F*) Functional analysis of vehicle-treated 25Q-Htt (black traces, bars) and 97Q-Htt (red traces, bars) neurons and HDACi RGFP109–treated 25Q-Htt (gray traces, bars) and 97Q-Htt (orange traces, bars) neurons. (*A*) Representative traces of evoked IPSCs. (*B* and *C*) Bar graphs showing mean evoked IPSC amplitudes (*B*) mean mIPSCs amplitudes (*C*). (*D*) Representative current traces of the response to a 5 s pulse of 500 mOsm hypertonic sucrose solution. (*E* and *F*) Bar graphs showing readily releasable pool size as measured by the charge of the transient response component (*E*) and mean vesicular probability (P_{vr}) (*F*). Data shown as mean ± SEM. Numbers in parentheses indicate sample sizes. One-way ANOVA or Kruskal–Wallis test coupled with Dunn's post hoc test: * refers to $P \leq 0.05$, ** $P \leq 0.01$, *** $P \leq 0.001$, and **** $P \leq 0.001$.

RNA-seq libraries from 117 single striatal GABAergic neurons and 14 astrocytes. All individual libraries showed high complexity with minor differences in variation (*SI Appendix*, Fig. S2*G*). In a cursory analysis, we found housekeeping genes such as *Actb* (beta-actin) and *Tubb3* (tubulin Bbeta 3 class III) were highly expressed in every single neuron (*SI Appendix*, Fig. S2 *C* and *D*). Additionally, GFP counts, indicating viral induction, were comparable across neuronal groups (*SI Appendix*, Fig. S2*E*). As expected, astrocytes only expressed *Actb*, as synapsin promoter–driven GFP and *Tubb3* expression are neuron specific (*SI Appendix*, Fig. S2 *C*–*E*). After exclusion of genes detected below five transcripts per kilobase million (tpm), we measured ~7,000 genes per cell, which is well in line with previously published Patch-seq datasets (23, 28) (*SI Appendix*, Fig. S2*F*).

When single neuronal (113) and astrocytic (14) transcriptomes were compared using the expression levels of a list of well-known markers, striatal GABAergic neurons were clearly distinguishable from astrocytes (Fig. 5*A*). As expected, pan-neuronal and inhibitory neuron genes including *Snap25* (synaptosome-associated protein 25), *Gad1* (glutamate decarboxylase 1), and *Gad2* (clutamate decarboxylase 2) were exclusively expressed in striatal GABAergic neurons but not in astrocytes. Excitatory neuron marker genes such as *Slc17a7* (vesicular glutamate transporter 1) and *Slc17a6* (vesicular glutamate transporter 2) did not appear in either population, while astrocytic markers were predominantly expressed in the astrocyte population. These observations together with the consistently high number of genes detected in each cell support the quality of the single-cell transcriptomic data in our study. Together with the aforementioned, unsupervised single-cell RNA-seq cluster analysis revealed that striatal transcription profile was clearly differentiated from astrocytes (Fig. 5*B*).

Analysis of Differential Gene Expression Reveals the Effects of Mutant Huntingtin Gene Expression and HDACi Treatment on Single Striatal Neuron Transcriptomes. To evaluate the effects of mutant *Htt* expression and HDACi treatment on the transcriptome of single striatal neurons, we searched for differentially expressed genes across four pair-wise comparisons: 1) 97Q-Htt neurons versus 25Q-Htt neurons, 2) RGPF109-treated 97Q-Htt neurons versus 25Q-Htt neurons, 3) RGPF109-treated 97Q-Htt neurons versus 97Q-Htt neurons, and 4) RGPF109-treated 25Q-Htt neurons versus 25Q-Htt neurons. We identified 1,475 differentially expressed genes (q-value < 0.1; IHW [independent hypothesis weighting] was used to corrected for multiple comparisons), between the 97Q-Htt and 25Q-Htt striatal neurons, of which 1,183 were down-regulated and 292 were up-regulated in 97Q-Htt neurons (Fig. 6*A* and Dataset S1). Gene Ontology (GO) analysis for these 1,183 down-regulated genes showed significant enrichment of numerous GO terms associated with synaptic transmission, signal transduction, regulation of neurotransmitter levels, and regulation of cytosolic calcium levels, indicating a disruption of key neuronal functions by 97Q-Htt expression in striatal neurons (Dataset S2). HD genes that are typically down-regulated in mouse models and in HD patients (19, 29), including *Drd2* (D[2] dopamine receptor), *Adora2a* (adenosine receptor), *Penk* (Preproenkephalin), and *Rasgrp1* (Ras guanyl releasing protein 1) were also found to be significantly down-regulated in 97Q-Htt neurons. On the other hand, GO analysis of the up-regulated genes resulted in enrichment of different biological processes such as protein autoubiquitination, sterol biosynthetic process, and defense response in 97Q-Htt neurons (Dataset S2). Notably, genes expressing several members of the heat shock protein family, including *Dnajb1* and *Dnajc11*, which play major roles in preventing protein aggregation, were among the up-regulated genes in 97Q-Htt neurons. The comparison of our single-cell RNA-seq data with a previously published list of 47 genes that are typically dysregulated in HD patients and mouse models (19, 29) revealed a highly significant overlap of the differentially-expressed genes, supporting the validity of our in vitro HD model and single-cell sequencing results (19 genes; hypergeometric test *P* value for the overlap; $P < 4.77e{-}07$; Dataset S3 and *SI Appendix*, Fig. S2*H*). Additionally, our findings on transcriptional changes

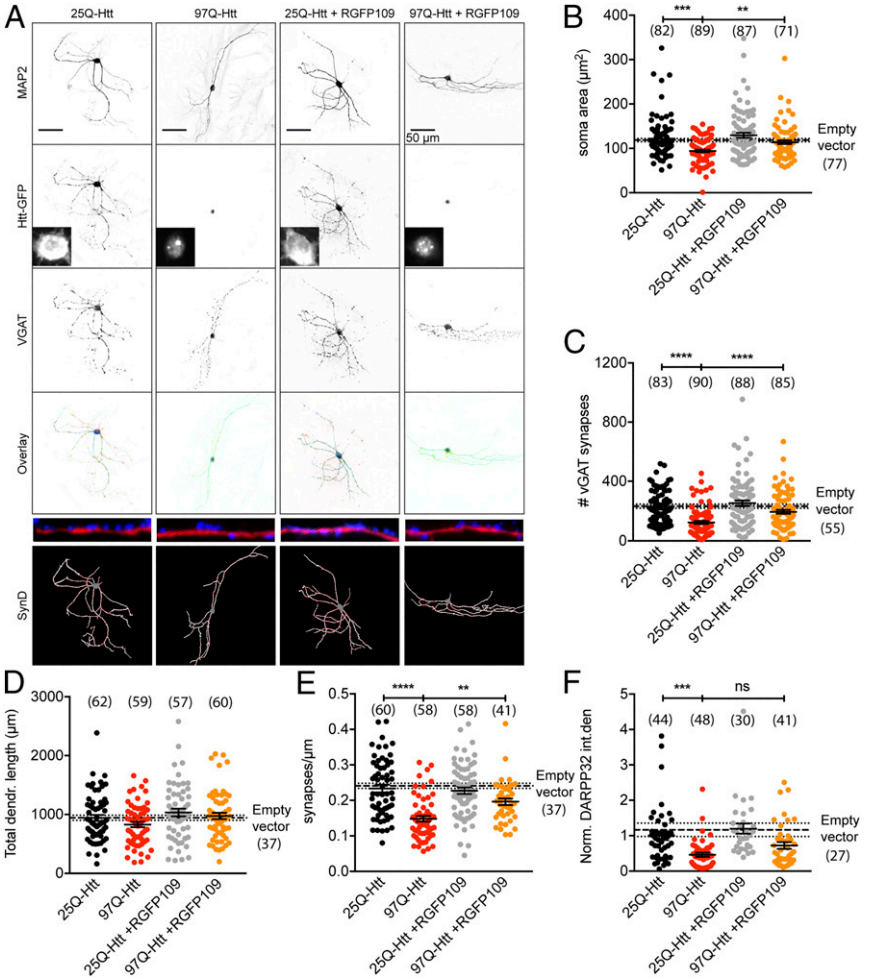

Fig. 4. Application of HDACi RGFP109 restores synapse number and soma size. (*A*) Representative images from vehicle-treated 25Q-Htt and 97Q-Htt neurons and HDACi RGFP109–treated 25Q-Htt and 97Q-Htt neurons showing immunoreactivity for MAP2, Htt-GFP, and VGAT and tracing of the same neurons with SynD. (*B–F*) Morphological analysis of 25Q-Htt (black bars) or 97Q-Htt (red bars) neurons. Bar graphs showing soma area (*B*), number of VGAT puncta per neuron (*C*), total length of dendrites (*D*), the number of VGAT puncta per µm of dendritic length (*E*), and normalized DARPP32 integrated density (*F*). Data shown as mean ± SEM. Numbers in parentheses indicate sample sizes. One-way ANOVA or Kruskal–Wallis test coupled with Dunn's post hoc test: * refers to $P \leq 0.05$, ** $P \leq 0.01$, *** $P \leq 0.001$, and **** $P \leq 0.001$.

between 97Q-Htt and 25Q-Htt neurons showed high similarities with our recently published bulk striatal RNA-seq data from the R6/1 mice at the age of 8 wk, which corresponds to an early HD stage when transcriptional dysregulation is dominated by expression changes of neuronal genes (20) (111 overlapping genes; hypergeometric test *P* value for the overlap; $P < 1.91e{-}04$; Dataset S3 and *SI Appendix*, Fig. S2*I*). Further, comparison of the list of differentially expressed genes between 97Q-Htt and 25Q-Htt neurons in our study with a recent cell type–specific transcriptomics dataset in indirect MSNs (iMSNs) and direct MSNs (dMSNs) in HD mouse striatum (30) showed a significant overlap of 306 commonly dysregulated genes as well as 160 and 145 genes that were uniquely dysregulated in dMSNs and iMSNs, respectively, in HD mouse striatum (*SI Appendix*, Fig. S3*A*). Notably, GO analysis of the commonly dysregulated genes revealed highly significant enrichments of GO terms that are related to synaptic signaling and transmission, indicating common dysregulation of these gene programs in dMSNs and iMSNs in HD. Dataset S8 provides GO analyses results and lists of the overlapping genes.

Next, the comparison of RGFP109- with vehicle- treated 97Q-Htt neuron transcriptomes revealed 1,014 differentially expressed genes (at q-value < 0.1), of which 196 showed lower expression and 818 higher expression values in RGFP109-treated 97Q-Htt neurons, indicating an overall up-regulating effect of HDACi (Fig. 6*A* and Dataset S1). Among the 1,014 differentially expressed genes by RGFP109 treatment, the expression profiles of 303 genes were also found to significantly differ between 97Q-Htt and 25Q-Htt neurons. Spearman's correlation between the fold changes of differentially expressed genes in 97Q-Htt versus 25Q-Htt and 97Q-Htt+RGFP109 versus 97Q-Htt revealed a significant anti-correlation ($r = -0.251$, $P < 0.001$), suggesting a counter effect of HDACi on the expression levels of genes that were dysregulated by the expression of mutant *Htt* in striatal neurons. Noteworthy, restoration effect by RGFP109 in down-regulated genes was associated with functions, such as the G protein–coupled receptor signaling pathway coupled to cyclic nucleotide second messenger, serotonin receptor signaling pathway, and calcium ion homeostasis. Likewise, genes associated with protein autoubiquitination and response to virus that were up-regulated in 97Q-Htt neurons restored their expression levels after RGFP109 treatment (Fig. 6*A*; log2FC heat map).

Further, to detect which genes are most robustly differentially expressed between the compared groups, we performed two types of permutation analyses followed by differential gene expression analysis. First, a random removal of 10% of the cells per group and, second, a random shuffling of the cell labels across compared

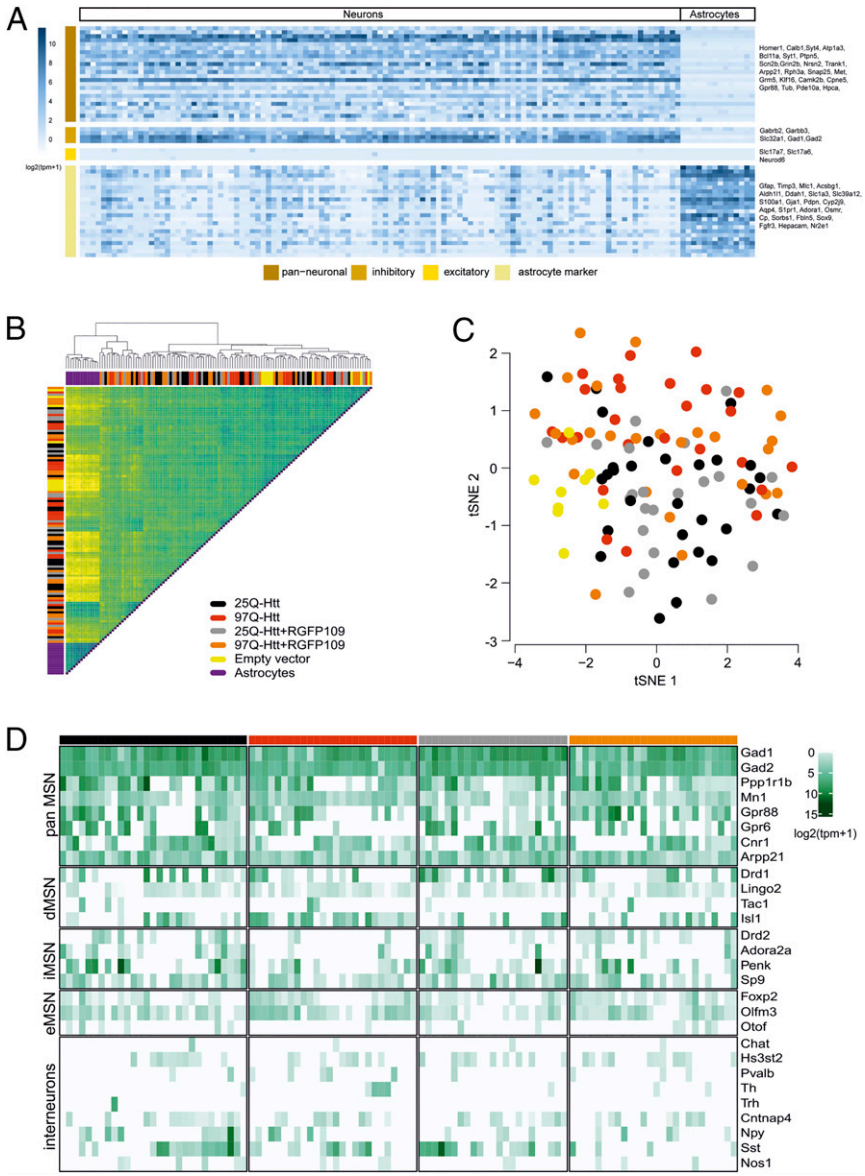

Fig. 5. Single-cell RNA-seq (Patch-seq) of striatal autaptic neurons. (*A*) Heat map illustrating gene expression profiles of pan-neuronal, inhibitory, excitatory, and astrocytic markers in all collected the samples. (*B*) Unsupervised hierarchical agglomerative clustering (Euclidean distance, complete linkage) of the cell–cell covariance matrix of the top 3,000 most variable genes, showing the presence of two groups (astrocytes and neurons). (*C*) t-distributed stochastic neighbor embedding (t-SNE) plot using the expression of the top 3,000 most variable genes in single-cell transcriptomes of five neuronal groups. Cells are colored according to the groups. (*D*) Heat map illustrating gene expression profiles of pan-MSN, direct MSN (dMSN), indirect MSN (iMSN), eccentric MSN (eMSN), and interneuron markers in all collected samples [based on dropviz.org database, (30, 62)].

groups were performed. In both analyses, 100 permutations were run followed by differential gene expression analysis. The overlap of these two analyses revealed 469 stably differentially expressed genes between the 97Q-Htt neurons and 25Q-Htt neurons (at a cutoff of ≥ 0.8 [80%] in the first and a cutoff of ≤ 0.2 [20%] in the second permutation). Among the 469 genes, which remain differentially expressed in 97Q-Htt–expressing neurons, were detected some of the aforementioned key HD genes, including *Drd2*, *Adora2a*, *Penk*, and *Rasgrp1*. The latter indicates their significant role in the dysregulation of 97Q-Htt neurons. The complete lists of these stably differentially expressed genes across all four pairwise comparisons are shown in Dataset S9 and *SI Appendix*, Fig. S4.

To investigate which pathways were affected by the expression of mutant *Htt* and HDACi treatment in single striatal neurons, we performed gene set enrichment analysis using WebGestalt (31) and analyzed all measured genes ranked based on their z-scores from single-cell differential expression (SCDE) analysis output. Our findings showed significant changes in the expression levels of 922 gene sets between 97Q-Htt and 25Q-Htt neurons (FDR < 0.25) (Dataset S4 and Fig. 6*B*). Strikingly, of the 922 gene sets, only 12 showed a positive enrichment in 97Q-Htt neurons, while the rest were negatively enriched. Of the 922 gene sets, HDACi treatment in 97Q-Htt neurons caused a counter effect on the enrichment of 892 gene sets, of which 275 were significant (Dataset S4 and Fig. 6*B*). Among the latter, we detected many gene sets typically related to neuronal functions, such as regulation of synaptic plasticity, regulation of GABAergic synaptic transmission, neurotrophin signaling pathways, and regulation of synaptic vesicle transport and exocytosis that were down-regulated in 97Q-Htt neurons and two gene sets associated with isoprenoid

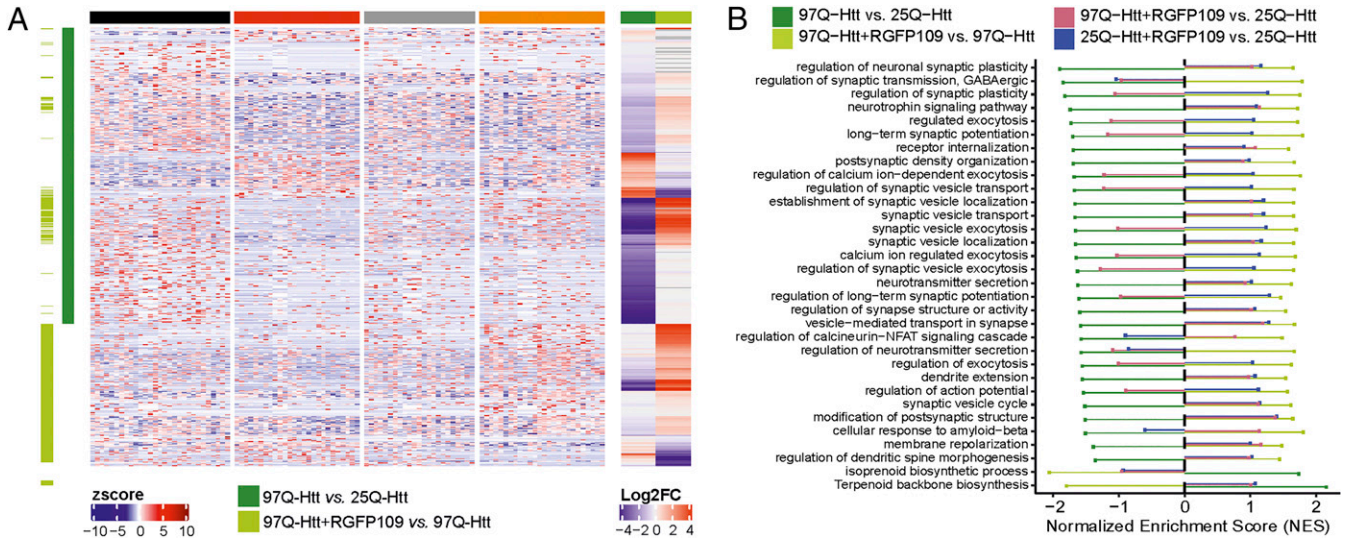

Fig. 6. Analysis of differential gene expression reveals the effects of mutant huntingtin gene expression and HDACi treatment on single striatal neuron transcriptomes. (*A*) Heat map of *z*-scores for differentially expressed genes for the four groups (25Q-Htt, black; 97Q-Htt, red; 25Q-Htt+RGFP109, gray; and 97Q-Htt+RGFP109, orange). The light and dark green bars in the left indicate the genes that are differentially expressed between 97Q-Htt and 25Q-Htt and between 97Q-Htt+RGFP109 and 97Q-Htt, respectively. The log2 fold changes (Log2FC) for 25Q-Htt versus 97Q-Htt and for 97Q-Htt+RGFP109 versus 97Q-Htt are also given. (*B*) A subset of enriched gene sets related to neuronal function for the four comparisons. The bars denote the normalized enrichment scores and the direction of expression change (up-regulated or down-regulated gene sets).

biosynthetic process and terpenoid backbone biosynthesis that were up-regulated in 97Q-Htt neurons. Together, these results indicate that 97Q-Htt causes a widespread impairment of neuronal gene expression programs, on which HDACi treatment exerts a largely restorative effect.

Linking Functional Data to Transcriptome (Patch-Seq). To identify genes whose differential expression is linked to deficits in synaptic transmission, we followed a two-step analysis approach. First, using the differentially expressed transcripts, we performed Spearman's correlation tests between gene expression levels and the electrophysiological parameters that showed the most significant differences between 97Q-Htt and 25Q-Htt neurons. We found 155, 187, and 268 differentially expressed genes that were significantly correlated with IPSC, RRP, and membrane capacitance, respectively ($P < 0.05$) (Dataset S5). Interestingly, we found 20 genes, including *Ddc*, *Atp2b2*, *Kcnmb4*, *Rasgrp1*, *Rasgrp2*, *Syt10*, and *Rdm1* that have been shown to be dysregulated in HD mice (19, 29), whose expression levels were significantly correlated with all three neuronal electrophysiological properties (Fig. 7*A* and Dataset S6). GO enrichment analysis of these genes revealed biological process terms involved mainly in neurotransmitter metabolic processes and response to calcium ions. Furthermore, for each 97Q-Htt neuron, we used the expression levels of all differentially expressed genes that were correlated to each electrophysiological parameter (IPSC, RRP, or membrane capacitance) to summarize the gene expression levels into a single expression index obtained from a principal component analysis. We then estimated the deviation of each 97Q-Htt neuron expression profile from the 25Q-Htt group as the mean Euclidean distance of the 97Q-Htt neuron from the former. The same analysis was carried out for each electrophysiological parameter where the mean distance was estimated. Correlation analysis between mean expression distances and shifts in IPSC ($r = 0.36$, $P = 0.07$), RRP ($r = 0.44$, $P = 0.04$), and membrane capacitance ($r = 0.17$, $P = 0.41$) showed a positive correlation, indicating that 97Q-Htt neurons that changed their expression profile more drastically had phenotypes further away from the 25Q-Htt neurons.

In regard to IPSC, significant biological process GO terms included response to amphetamine, positive regulation of transport, positive regulation of secretion, regulation of protein localization, G protein–coupled receptor signaling pathway, regulation of long-term synaptic potentiation and regulation of neurotransmitter levels (Dataset S7*A*). The strongest positive correlation ($r = 0.485$) between gene expression levels and IPSC was detected for *Gpr12* (G protein coupled receptor 12 gene), followed by *Ddc*, *Atp2b2*, *Glp2r*, and *Kcnmb4*. Notably, the expression levels of key HD genes that are typically dysregulated across models and HD patients including *Kalm*, *Adora2a*, *Drd2*, *Rasgrp1*, *Rasgrp2*, and *Mapk4* were also found to be significantly positively correlated with IPSC. On the other hand, the *Rtp4* gene showed the strongest negative correlation to IPSC ($r = -0.51$), followed by *Acly*, *Usp18*, *Sqle*, and *Sfmbt2*.

Correlation analysis between the expression levels of differential transcripts and RRP changes revealed the strongest positive correlation for *Rasgrp2* ($r = 0.5$), followed by *Trp53*, *Tmem158*, *Mchr1*, *Tbl1x*, *Snx25*, and *Gast*, while *Sfmbt2* ($r = -0.49$) showed the strongest negative correlation, followed by *Spata9*, *Hmgcr*, *Cd81*, *Rdm1*, and *Kri1*. Biological process GO terms associated with these genes were related to synapse signaling and organization, GABAergic synaptic transmission, anterograde transsynaptic signaling, and chemical synaptic transmission (Dataset S7*B*).

Finally, membrane capacitance, an electrophysiological parameter indicative of cell size that is significantly changed in mutant Htt neurons, was linked to genes associated with BP GO terms involved in the regulation of cGMP-mediated signaling, regulation of modification of synaptic structure, synapse organization, and adenylate cyclase–modulating G protein–coupled receptor signaling pathway (Dataset S7*C*). The strongest positive and negative correlations were observed for *Camkv* ($r = 0.475$; a typical HD gene) and for *Hmmr* ($r = -0.528$) and *Psmb9* ($r = -0.443$), respectively. Other highly correlated genes observed were *Lrguk*, *Kctd12*, *Baiap2*, *Etv1*, *Rasgrp2*, and *Atp2b2*.

In the second step of our analysis, we tested whether the single-neuron gene expression data obtained herein could predict neuronal electrophysiological properties and the changes in their states in 97Q-Htt neurons. To do so, for each electrophysiological parameter across neurons, we trained one machine learning model

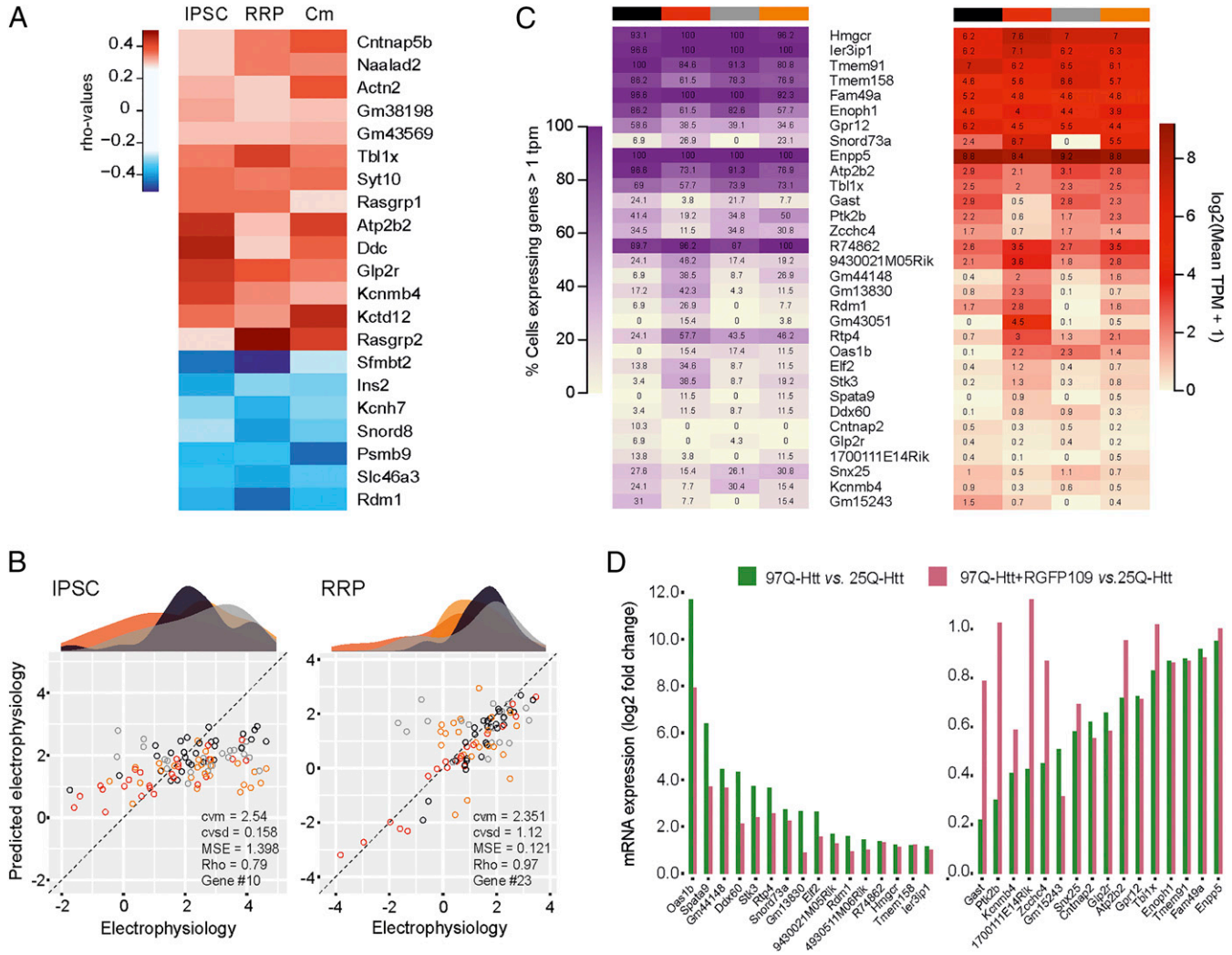

Fig. 7. Linking functional and transcriptome data. (*A*) Heat map of Spearman's rho values for common HD genes for the three electrophysiological parameters (IPSC, RRP, and membrane capacitance) that showed the most significant differences between 25Q-Htt and 97Q-Htt neurons. (*B*) Scatter plots showing the performance of the generalized linear model using single-cell gene expression data to predict neuronal electrophysiological properties IPSC and RRP, based on the expression levels of 10 and 23 genes, respectively. For each model, the cvm (mean cross-validation error), cvsd (cross-validation SE), and MSE (mean square error) are provided. Individual neurons are color coded according to their groups (25Q-Htt, black; 97Q-Htt, red; 25Q-Htt+RGFP109, gray; and 97Q-Htt+RGFP109, orange). The values given in the figures are achieved from machine learning results applied to 25Q-Htt and 97Q-Htt neurons. Other neurons were added to the plot for the purpose of visualization. (*C*) Heat maps of the 33 genes that could predict the states of the electrophysiological properties IPSC ($r = 0.79$) and RRP ($r = 0.97$). The left heat map shows the percentage of cells expressing each gene and the right heat map the expression levels of those genes. (*D*) Bar plots showing the levels of differential expression as a log2 fold change between 97Q-Htt versus 25Q-Htt and between 97Q-Htt+RGFP109 versus 25Q-Htt for the genes predicted by GLM. Left graph: up-regulated in 97Q-Htt neurons. Right graph: down-regulated in 97Q-Htt neurons.

using the differentially expressed genes that were significantly correlated with the given function. Our findings showed that the states of IPSC and RRP could be predicted with high correlation ($r = 0.79$ and $r = 0.97$, respectively; Fig. 7*B*) using the differential expression levels of 10 and 23 genes, respectively (Fig. 7*C* and Dataset S6). Notably, these 33 genes were the result of three unbiased analyses that we performed on our dataset, that of differential gene expression (Fig. 6*A*), Spearman correlation (Dataset S5), and generalized linear model (GLM) (Fig. 7*C*). Interestingly, while all these 33 genes contributed to the prediction of the states of IPSC and RRP (Dataset S6), we observed a significant anti-correlation between the gene frequency (Fig. 7*C*) and gene weight in the machine learning results (Dataset S6) (rho = −0.6, $P = 2 \times 10^{-04}$), indicating that those genes with low frequency expression had a higher impact on the prediction. Lastly, this model showed weak prediction for membrane capacitance. This may indicate that factors beyond differential gene expression contribute to decreased membrane capacitance in 97Q-Htt neurons or that the difference in this property between groups is too small to predict from single-cell gene expression data. It is of note that our initial attempts using top variable genes or all expressed genes in our data resulted in weak or no association between gene expression and electrophysiological properties and that the use of differentially expressed genes as input for the correlation and GLM analyses was key for identification of these 33 genes, which accurately predict the IPSC and RRP states in our study.

Among the 33 genes detected by the GLM, we identified a number of genes, including *Atp2b2*, *Kcnmb4*, *Cntnap5b*, *Glp2r*, and *Rdm1*, whose expression levels significantly correlated with all electrophysiological properties (i.e., RRP, IPSC, and membrane capacitance). It is worth noting that in our recent study using bulk tissue RNA-seq (20), we detected 22 out of these 33 genes in the striatum of R6/1 transgenic mouse, and among these, 11 genes showed concordant expression changes between HD mice and the single neurons examined in the present study. These genes are

Fam49a, *Rtp4*, *Gpr12*, *Ptk2b*, *Kcnmb4*, *Snx25*, *Atp2b2*, *Spata9*, *Stk3*, *Rdm1*, and *Ier3ip1*. While our previous work showed their dysregulation in HD mouse striatum, the current study provides evidence linking their altered expression to specific neuronal functional deficits in HD. Moreover, the comparison of these 33 genes with recently published RNA-seq datasets revealed that 24 out of 33 genes were previously shown to be differentially expressed in HD mice and patient brain, while five of these, *Gpr12* (32), *Stk3* (33), *Hmgcr* (34), *Atp2b2* (35), and *Ptk2b* (36), were suggested to exert beneficial effects on disease features of HD (Dataset S10).

Further, to infer the pathway level information and interpret the collective functions of these genes, we leveraged a network analysis method. We used these 33 genes as the seeds to construct a subnetwork that connects these genes either directly or with the help of intermediate proteins. By merging all-pair shortest paths between seed proteins, we obtained a compact subnetwork that includes 172 interactions between 68 proteins of which 50 are intermediate proteins and 18 are among the 33 seed genes (*SI Appendix*, Fig. S5). GO analysis revealed enrichments of GO biological process terms that are relevant to HD pathology, such as regulation of gene expression, virus response, regulation of cell growth, and neuron projection development (Dataset S11).

Given our earlier evidence that inhibition of HDAC1/3 reverses phenotypes in 97Q-Htt neurons, we next investigated whether RGFP109 treatment can restore the expression levels of these 33 genes, whose dysregulation was linked to the functional deficits in 97Q-Htt neurons. Our analysis revealed 24 genes (72%) whose expression levels shifted toward 25Q-Htt levels (Fig. 7*D*). While some of these genes have previously been associated with HD, such as *Ptk2b* (36), *Atp2b2* (37), *Tbl1x* (38), *Kcnmb4* (39), *Stk3* (33), and *Rtp4* (40), many of them (e.g., *Zcchc4*, *Snx25*, and *Rdm1*) have not been investigated regarding their roles in HD pathogenesis or in the regulation of synaptic function. Altogether, our findings verify previous studies but also reveal previously unknown candidate genes whose dysregulation is associated to specific neuronal functional deficits in HD pathology.

Discussion

Although it is now clear that mutant Htt protein induces neuronal dysfunction mostly through the nuclear accumulation of polyglutamine fragments and the abnormal interaction with its partners (14, 41), we still know surprisingly little about its effect on striatal synapse function. Using lentivirus-mediated delivery of mutant *Htt* in primary autaptic striatal cultures and single-cell transcriptomics, this study provides insights in to pathophysiological and molecular aspects of HD. First, we showed that mutant Htt decreases synaptic output of striatal neurons in a cell-autonomous fashion. Second, using the single-cell RNA sequencing technique, Patch-seq, we identified a number of genes that were significantly dysregulated in mutant Htt neurons and displayed differential expression that was correlated with deficiencies in physiology (Fig. 7 and Dataset S5). Finally, we could show that inhibiting HDAC1/3 activity in mutant Htt neurons not only rectified several functional and morphological deficits but also to some extent restored the dysregulated transcriptional profile. These findings provide evidence that epigenetic mechanisms play an essential role in the pathophysiology of HD and support their beneficial effects for therapy.

In normal conditions, Htt in axonal terminals interacts with synaptic vesicle proteins maintaining neurotransmitter release (42). The expansion of polyglutamine tract of Htt, however, influences its binding affinity, resulting in neuropathological changes (14). In our in vitro HD model, expression of the expanded 97Q-Htt reduced the evoked response amplitude through the decrease of spontaneous activity and the size of a readily releasable vesicle pool (Fig. 1). These findings were also reflected in morphological changes, measured as a decrease in GABAergic synapse number (Fig. 2*C*). As no changes in release probability and short-term plasticity were observed in 97Q-Htt neurons (Fig. 1 *M* and *N*), Htt likely plays no role in determining the efficacy of single-vesicle release. Consistent with these results, MSN connectivity and evoked responses are decreased in symptomatic mice of the R6/2 HD mouse model (43). Membrane capacitance and soma size were also significantly decreased in mutant Htt neurons, while a similar though not significant trend was observed for dendrite growth (Figs. 1*E* and 2 *B* and *D*). Taken together, our results are in line with previous studies in HD mice showing that Htt mutation drove a reduction in membrane capacitance (44), soma size, dendritic length (45, 46), and the number of dendritic spines (11). Overall, our in vitro model system recapitulates morphological phenotypes observed in HD mouse models.

Our study combines electrophysiological and transcriptional analyses of individual cells, bridging the gap between physiological and molecular processes in a disease state at the single-neuron level. The significant differences in gene expression between 97Q-htt and 25Q-Htt neurons indicate that Htt directly or indirectly interacts with transcription factors and regulators, modulating the expression of downstream genes. Unbiased cluster analysis indicated the presence of two major clusters, one comprising from astrocytes and the other one from neurons. Within neuronal cluster, no further subclustering was observed among the different phenotypic groups (Fig. 5*B*). The latter indicates that the observed differences are not due to differences in housekeeping genes (*SI Appendix*, Fig. S2 *C* and *D*) but rather to differences in specific gene expression programs triggered by *Htt* mutation. Differential expression analysis identified 1,475 transcripts, the majority of which were involved in cell growth, synaptic transmission, gene expression regulation–related signal transduction, regulation of neurotransmitter levels, and regulation of cytosolic calcium levels. All of these pathways play a key role in synapse formation and function. One of the mechanisms, via which mutant Htt causes transcriptional dysregulation, is the sequestration of key transcription factors and regulators such as TBP and CBP (47, 48) into nuclear mutant Htt aggregates, a key hallmark of HD pathology that we observed also in our model (Figs. 1*A* and 2*A*). Therefore, a possible mechanism to explain the synaptic phenotypes observed in our study could involve the impairment or sequestration of the transcriptional regulators that control gene programs related to synapse function and formation by mutant Htt aggregates. Furthermore, a number of key genes characteristic of HD were detected, such as the *Drd2*, which is expressed in MSNs and involved in the modulation of locomotion, memory, and learning (49), and the *Adora2a*,which is important for the modulation of synaptic activity and the proper function of brain-derived neurotrophic factor, a factor that is essential for the survival of neurons in HD (50) and growth (51). Similarly, we found decreased expression of *Penk* that controls striatal motor activity in mice (52) and *Rasgrp1* but up-regulation of *Dnajb1* and *Dnajc11*, two heat shock proteins that promote protein folding and prevent misfolded protein aggregation (53, 54). It is of note that almost 80% of the differentially expressed genes were down-regulated in 97Q-Htt neurons indicating an overall disruption of gene expression programs by mutant *Htt* expression in striatal neurons (55).

A recent study utilizing the translating ribosome affinity purification (TRAP) technology for in-depth profiling of cell type–specific changes in two HD mouse models revealed that the most significant gene pathways commonly dysregulated in direct and indirect MSNs, as well as in corticostriatal projection neurons, were related to the regulation of synaptic transmission and function (30). Herein, by applying Patch-seq (23) to an HD model, we could directly study the relation between transcriptional changes and the functional deficits resulting from mutant *Htt* expression in single striatal neurons. We identified down-regulation of transcripts that were associated with the regulation of neurotransmitter levels, transsynaptic signaling, and protein–protein interactions and whose expression levels were positively correlated with alterations in synaptic strength (e.g., *Kalrn*, *Adora2a*, *Syt10*, *Atp2b2*, and *Kcnmb4*), RRP (e.g., *Rasgrp1-2*, *Stk3*, and *Syt10*), and membrane capacitance (e.g., *Camkv* and *Rasgrp2*).

Remarkably, our linear model showed that, the differential transcriptional profiles of individual striatal neurons were able to predict their electrophysiological properties, and these predicted values are highly correlated with the measured electrophysiological properties ($r = 0.79$ for IPSC, $r = 0.97$ for RRP). Overall, our Patch-seq data suggest a tight transcription–phenotype relationship in which mutant Htt neurons with milder gene expression alterations have phenotypes closer to wild-type, while stronger down-regulation in these genes leads to a more severe HD phenotype.

The involvement of epigenetic transcriptional regulation in HD and the ability to selectively inhibit these processes make transcriptional regulators, such as HDAC enzymes, attractive targets to alleviate HD progression. Mouse models of HD suggest that the HDAC1 and HDAC3 subtypes, but not HDAC2, HDAC4, and HDAC7, predominately shift to nuclear localization in an HD-dependent manner, possibly leading to chromatin compaction and a more transcriptionally silenced state (56). Supporting this, an HDAC1/3-specific inhibitor was found to significantly prevent body weight loss and improve motor cognition in N171-82Q transgenic HD mice (57). In agreement with these studies, we found RGFP109, a specific inhibitor for HDAC1/3, could effectively restore deficits in synaptic function and morphology of 97Q-Htt striatal neurons and alleviate the expression levels of dysregulated genes. We found that RGFP109 treatment showed a restorative effect on the expression levels of 30% of the genes that were differentially expressed between 97Q-Htt and 25Q-Htt neurons, including key HD genes and those whose dysregulation was linked to functional deficits. Among machine learning–identified genes that were linked to the neuronal deficits, the strongest repair effect of RGFP109 treatment was observed on the expression of *Ptk2b*, a gene linked to RRP size based on our machine learning results. *Ptk2b* encodes for Pyk2 protein, a nonreceptor calcium-dependent tyrosine kinase with a role in synaptic plasticity (58, 59). Importantly, Pyk2 overexpression was recently shown to provide therapeutic effects on several features of HD in the R6/1 transgenic mice model (36). Likewise, gene set enrichment analysis identified a number of differentially enriched processes that were associated with the regulation of neuronal synaptic plasticity, GABAergic synaptic transmission, and neurotrophin signaling pathway and regulation of synaptic vesicle transport and exocytosis. In our in vitro system, this could explain the increase that we observed in evoked IPSC, RRP size, synapse number, and soma size in 97Q-Htt after RGFP109 application. These results highlight the role of transcriptional dysregulation as a pivotal disease mechanism in leading to neuronal dysfunction in HD and provide supporting evidence for its targeting as a valuable therapeutic strategy in HD and potentially other neurological diseases with convergent molecular disease mechanisms.

Overall, our study extends beyond the descriptive analyses of gene expression changes and synaptic transmission deficits in HD to identify certain gene–function relationships that provide insights into HD pathophysiology and underlying mechanisms. Future work will undertake the task of validating the specific genes and gene sets linked to functional deficits in mutant Htt as well as revealing their potential to serve as targets for HD therapy.

Methods

Mice and Cell Culture. Animal housing and use were in compliance with and approved by the Animal Welfare Committee of Charité Medical University and the Berlin State Government Agency for Health and Social Services. Newborn C57BLJ6/N mice (P0 to P1) of both sexes were used for all the experiments.

Primary striatal neuronal cultures were prepared as described previously by Arancillo et al. (60). Briefly, neurons were seeded and cultured on microisland astrocyte feeder layers that were prepared 1 to 2 wk before the neuronal culture preparation. Astrocytes derived from C57BLJ6/N mouse cortices (P0 to P1) were plated on collagen/ poly-D-lysine microislands made on agarose-coated coverslips using a custom-built rubber stamp to achieve uniform size (200 μm diameter). For all experiments, striatal neurons were then digested with papain (Worthington) and plated on astrocytes at a density of 3,500 neurons per 35 mm dish and grown in a chemically defined medium (neurobasal-A medium supplemented with glutamax and B-27; Invitrogen). Under these conditions, a single neuron on an astrocyte microisland forms recurrent synapses called autapses (22).

Electrophysiology. Whole-cell voltage clamp recordings were performed on striatal autaptic neurons between DIV 12 and 15 and held at −70 mV with a Multiclamp 700B amplifier (Molecular Devices) under the control of Clampex 10.2 (Molecular Devices). Data were digitally sampled at 10 kHz and low-pass Bessel filtered at 3 kHz with an Axon Digidata 1440A digitizer (Molecular Devices). Series resistance was compensated at 70%, and only cells with <12 MOhm resistance were included. All experiments were performed at room temperature (23 to 24 °C). Infected neurons were identified by a GFP-positive signal. To minimize variability among datasets, an approximately equal number of cells were recorded from all groups on a given experimental day.

During recordings, neurons were immersed in standard extracellular solution consisting (in millimoles) by: 140 NaCl, 2.4 KCl, 10 Hepes, 10 glucose, 4 $MgCl_2$, and 2 $CaCl_2$. The patch pipette internal solution contained the following (in millimoles): 136 KCl, 17.8 Hepes, 1 EGTA, 0.6 MgCl2, 4 ATP-Mg, 0.3 GTP-Na, 12 phosphocreatine, and 50 U/mL phosphocreatine kinase. Both solutions were adjusted to pH 7.4 with osmolarity at 300 mOsm. Hypertonic sucrose solution was prepared as 500 mM sucrose in standard extracellular solution (27). Solutions were applied using a fast-flow system that provides rapid exchange at time constants of ∼20 to 30 ms. Borosilicate glass patch pipettes were pulled using a multistep puller (P-87, Sutter Instruments) using conditions that kept pipette tip resistance between 2 and 5 MΩ.

Action potential–evoked PSCs were triggered by a 2 ms somatic depolarization from −70mV to 0 mV. Neurons were stimulated at 0.1 Hz in standard external solution to measure basal-evoked IPSCs. The kinetics of the evoked response and GABA receptor antagonist (30 μM bicuculline; Tocris Bioscience) were used in order to verify glutamatergic or GABAergic identities. Spontaneous release was determined by detecting mIPSCs for 20 to 40 s at −70 mV with the help of a template-based algorithm in Axograph X. The threshold for detection was set at three times the baseline SD from a template of 0.5 ms rise time and 18 ms decay for GABAergic events. The averages of the traces recorded in the presence of bicuculline were filtered at 1 kHz and subtracted from the average of the filtered traces recorded in the external solution without bicuculline to cancel electrical noise. Membrane capacitance measurements were obtained from the membrane test function in pClamp. RRP size was assessed by measuring the charge transfer of the transient synaptic current induced by a 5 s application of 500 mM sucrose in standard extracellular solution (27). The number of synaptic vesicles in the RRP of each neuron was calculated by dividing the sucrose charge by the charge of the average miniature event. Similarly, the release probability of a single synapse (P_{vr}) was calculated as the ratio of evoked response charge to RRP charge. Short-term plasticity was examined either by evoking 50 synaptic responses at 5 Hz or 2 IPSC responses with an interstimulus interval of 50 ms to measure paired-pulse ratio (PPR). PPR was determined by calculating the ratio of IPSC amplitude of second over the first synaptic response. Data were analyzed in Axograph X (Axograph Scientific), Excel (Microsoft) and Prism (GraphPad).

Single-Cell Collection and cDNA Preparation. Following electrophysiological recording at DIV15, single striatal GABAergic neurons were collected immediately by applying light negative pressure through the same glass patch pipette. Only samples (cells) whose entire somatic compartment, including their nucleus, were visibly aspirated into the micropipette were further processed. Following successful aspiration, the sample was transferred in a volume of <2 μL of internal patch solution into a RNase-free PCR tube containing 1 μL Lysis buffer, supplemented with RNase inhibitor, according to SMARTer Ultra Low RNA Kit (Clontech). To eject the content of the patch pipette, the recording pipette was pulled out from the recording chamber, and the tip of the electrode was broken against the inside wall of the collecting tube. Collected single cells were immediately spun down at room temperature and put on dry ice until −80 °C storage. SMARTer cDNA synthesis was performed using SMARTer Ultra Low RNA Kit according to manufacturer's protocol.

In brief, first-strand cDNA was synthesized from poly(A)+ RNA by incubation with 1 μL of 3′ SMART CDS (cDNA synthesis) Primer II A (24 μM) for 3 min at 72 °C, followed by reverse transcription in a 20 μL final reaction volume using 200 units of SMARTScribe Reverse Transcriptase for 90 min at 42 °C and inactivation for 10 min at 70 °C. First-strand cDNA was then used as template for second-strand cDNA synthesis which subsequently amplified using the following PCR thermocycler program: 95 °C for 1 min, 17 cycles of 95 °C for 15 s, 65 °C for 30 s, 68 °C for 6 min, and 72 °C for 10 min. PCR-amplified double-stranded cDNA was immobilized onto Agencourt AMPure XP SPRI Beads (Beckman Coulter Genomics), purified by two washes in 80% ethanol, and eluted in 12 μL of purification buffer (Clontech). The quality of the samples

was assessed with Agilent 2100 Bioanalyzer High Sensitivity DNA Kit (Agilent Technologies).

In general, we aimed to collect approximately equal cell numbers of each group from each experiment. Based on previous published Patch-seq experiments, ~25 samples per group seem to be sufficient to discriminate differences between groups.

Statistical Analysis. Unless specified otherwise, data are presented as means ± SEM. For statistical analysis, D'Agostino–Pearson test was carried out to test whether data were normally distributed. Student's *t* test for independent groups and one-way ANOVA using Tukey's honest significant difference post hoc test were used to assign statistical significances between conditions. If parametric assumptions were violated, Mann–Whitney *U* test and Kruskal–Wallis test coupled with Dunn's post hoc test were performed.

Data Availability. RNA-seq data have been deposited in the Gene Expression Omnibus (GEO) database under the accession number GSE171099 (61).

ACKNOWLEDGMENTS. F.P. was funded by a predoctoral fellowship from the NeuroCure Cluster of Excellence. This work was funded by the NeuroCure Cluster of Excellence Exc 257 funding (F.Y. and C.R.) and by German Research Council Grants SFB665/B11 and RO1296/12-1 (C.R.). We thank Christoph Harms for help with initial generation of mutant and wild-type Htt-expressing lentiviruses and Bettina Brokowski, Rike Dannenberg, Berit Söhl-Kielczynski, Heike Lerch, Belgin Cansin Peksen, Miriam Petzold, and Katja Pötschke for technical assistance. We acknowledge the Scientific Genomics Platforms at the Max Delbrück Center for Molecular Medicine Berlin and at the Berlin Institute of Health for sequencing RNA-seq libraries. We also thank Melissa A. Herman and David E. Housman for critically reading and insightful comments on the manuscript.

1. J. P. Vonsattel, M. DiFiglia, Huntington disease. *J. Neuropathol. Exp. Neurol.* **57**, 369–384 (1998).
2. G. A. Graveland, M. DiFiglia, The frequency and distribution of medium-sized neurons with indented nuclei in the primate and rodent neostriatum. *Brain Res.* **327**, 307–311 (1985).
3. J. M. Kemp, T. P. S. Powell, The structure of the caudate nucleus of the cat: Light and electron microscopy. *Philos. Trans. R. Soc. Lond. B Biol. Sci.* **262**, 383–401 (1971).
4. H. D. Rosas *et al*., Cerebral cortex and the clinical expression of Huntington's disease: Complexity and heterogeneity. *Brain* **131**, 1057–1068 (2008).
5. The Huntington's Disease Collaborative Research Group, A novel gene containing a trinucleotide repeat that is expanded and unstable on Huntington's disease chromosomes. *Cell* **72**, 971–983 (1993).
6. J. P. Vonsattel *et al*., Neuropathological classification of Huntington's disease. *J. Neuropathol. Exp. Neurol.* **44**, 559–577 (1985).
7. L. A. Raymond *et al*., Pathophysiology of Huntington's disease: Time-dependent alterations in synaptic and receptor function. *Neuroscience* **198**, 252–273 (2011).
8. G. A. Garden, A. R. La Spada, Intercellular (mis)communication in neurodegenerative disease. *Neuron* **73**, 886–901 (2012).
9. J. Y. Li, M. Plomann, P. Brundin, Huntington's disease: A synaptopathy? *Trends Mol. Med.* **9**, 414–420 (2003).
10. M. DiFiglia *et al*., Aggregation of huntingtin in neuronal intranuclear inclusions and dystrophic neurites in brain. *Science* **277**, 1990–1993 (1997).
11. P. Guidetti *et al*., Early degenerative changes in transgenic mice expressing mutant huntingtin involve dendritic abnormalities but no impairment of mitochondrial energy production. *Exp. Neurol.* **169**, 340–350 (2001).
12. M. DiFiglia *et al*., Huntingtin is a cytoplasmic protein associated with vesicles in human and rat brain neurons. *Neuron* **14**, 1075–1081 (1995).
13. A. J. Morton, R. L. M. Faull, J. M. Edwardson, Abnormalities in the synaptic vesicle fusion machinery in Huntington's disease. *Brain Res. Bull.* **56**, 111–117 (2001).
14. S. H. Li, X. J. Li, Huntingtin-protein interactions and the pathogenesis of Huntington's disease. *Trends Genet.* **20**, 146–154 (2004).
15. J. H. Cha *et al*., Altered brain neurotransmitter receptors in transgenic mice expressing a portion of an abnormal human Huntington disease gene. *Proc. Natl. Acad. Sci. U.S.A.* **95**, 6480–6485 (1998).
16. R. Luthi-Carter *et al*., Decreased expression of striatal signaling genes in a mouse model of Huntington's disease. *Hum. Mol. Genet.* **9**, 1259–1271 (2000).
17. R. Luthi-Carter, J. H. J. Cha, Mechanisms of transcriptional dysregulation in Huntington's disease. *Clin. Neurosci. Res.* **3**, 165–177 (2003).
18. P. Langfelder *et al*., Integrated genomics and proteomics define huntingtin CAG length-dependent networks in mice. *Nat. Neurosci.* **19**, 623–633 (2016).
19. M. Vashishtha *et al*., Targeting H3K4 trimethylation in Huntington disease. *Proc. Natl. Acad. Sci. U.S.A.* **110**, E3027–E3036 (2013).
20. F. Yildirim *et al*., Early epigenomic and transcriptional changes reveal Elk-1 transcription factor as a therapeutic target in Huntington's disease. *Proc. Natl. Acad. Sci. U.S.A.* **116**, 24840–24851 (2019).
21. A. Hodges *et al*., Regional and cellular gene expression changes in human Huntington's disease brain. *Hum. Mol. Genet.* **15**, 965–977 (2006).
22. J. M. Bekkers, C. F. Stevens, Excitatory and inhibitory autaptic currents in isolated hippocampal neurons maintained in cell culture. *Proc. Natl. Acad. Sci. U.S.A.* **88**, 7834–7838 (1991).
23. C. R. Cadwell *et al*., Electrophysiological, transcriptomic and morphologic profiling of single neurons using Patch-seq. *Nat. Biotechnol.* **34**, 199–203 (2016).
24. T. Zhang, S. Cooper, N. Brockdorff, The interplay of histone modifications–Writers that read. *EMBO Rep.* **16**, 1467–1481 (2015).
25. J. Del Castillo, B. Katz, Quantal components of the end-plate potential. *J. Physiol.* **124**, 560–573 (1954).
26. C. F. Stevens, Neurotransmitter release at central synapses. *Neuron* **40**, 381–388 (2003).
27. C. Rosenmund, C. F. Stevens, Definition of the readily releasable pool of vesicles at hippocampal synapses. *Neuron* **16**, 1197–1207 (1996).
28. C. Bardy *et al*., Predicting the functional states of human iPSC-derived neurons with single-cell RNA-seq and electrophysiology. *Mol. Psychiatry* **21**, 1573–1588 (2016).
29. T. Seredenina, R. Luthi-Carter, What have we learned from gene expression profiles in Huntington's disease? *Neurobiol. Dis.* **45**, 83–98 (2012).
30. H. Lee *et al*., Cell type-specific transcriptomics reveals that mutant huntingtin leads to mitochondrial RNA release and neuronal innate immune activation. *Neuron* **107**, 891–908.e8 (2020).
31. Y. Liao, J. Wang, E. J. Jaehnig, Z. Shi, B. Zhang, WebGestalt 2019: Gene set analysis toolkit with revamped UIs and APIs. *Nucleic Acids Res.* **47**, W199–W205 (2019).
32. E. Murillo-Rodriguez, J. M. Monti, S. R. Pandi-Perumal, Eds. *Cannabinoids and Neuropsychiatric Disorders*, (Springer International Publishing, 2021).
33. S.-P. Riechers *et al*., Interactome network analysis identifies multiple caspase-6 interactors involved in the pathogenesis of HD. *Hum. Mol. Genet.* **25**, 1600–1618 (2016).
34. R. Kacher *et al*., CYP46A1 gene therapy deciphers the role of brain cholesterol metabolism in Huntington's disease. *Brain* **142**, 2432–2450 (2019).
35. E. E. Strehler, S. A. Thayer, Evidence for a role of plasma membrane calcium pumps in neurodegenerative disease: Recent developments. *Neurosci. Lett.* **663**, 39–47 (2018).
36. A. Giralt *et al*., Pyk2 modulates hippocampal excitatory synapses and contributes to cognitive deficits in a Huntington's disease model. *Nat. Commun.* **8**, 15592 (2017).
37. A. Kuhn *et al*., Mutant huntingtin's effects on striatal gene expression in mice recapitulate changes observed in human Huntington's disease brain and do not differ with mutant huntingtin length or wild-type huntingtin dosage. *Hum. Mol. Genet.* **16**, 1845–1861 (2007).
38. L. Francelle, "A study of striatal markers as disease modifiers in Huntington's disease," Doctroral thesis, Université Paris Sud - Paris XI, Orsay, France (2014).
39. D. Kuljis, T. Kudo, Y. Tahara, C. A. Ghiani, C. S. Colwell, Pathophysiology in the suprachiasmatic nucleus in mouse models of Huntington's disease. *J. Neurosci. Res.* **96**, 1862–1875 (2018).
40. X. Dong, S. Cong, Identification of differentially expressed genes and regulatory relationships in Huntington's disease by bioinformatics analysis. *Mol. Med. Rep.* **17**, 4317–4326 (2018).
41. S. W. Davies *et al*., Formation of neuronal intranuclear inclusions underlies the neurological dysfunction in mice transgenic for the HD mutation. *Cell* **90**, 537–548 (1997).
42. A. L. Proskura, S. O. Vechkapova, T. A. Zapara, A. S. Ratushniak, Protein-protein interactions of huntingtin in the hippocampus [in Russian]. *Mol. Biol. (Mosk.)* **51**, 734–742 (2017).
43. C. Cepeda *et al*., Multiple sources of striatal inhibition are differentially affected in Huntington's disease mouse models. *J. Neurosci.* **33**, 7393–7406 (2013).
44. C. Cepeda *et al*., NMDA receptor function in mouse models of Huntington disease. *J. Neurosci. Res.* **66**, 525–539 (2001).
45. M. S. Levine *et al*., Enhanced sensitivity to N-methyl-D-aspartate receptor activation in transgenic and knockin mouse models of Huntington's disease. *J. Neurosci. Res.* **58**, 515–532 (1999).
46. M. A. Ariano *et al*., Striatal potassium channel dysfunction in Huntington's disease transgenic mice. *J. Neurophysiol.* **93**, 2565–2574 (2005).
47. F. C. Nucifora *et al*., Interference by huntingtin and atrophin-1 with CBP-mediated transcription leading to cellular toxicity. *Science* **291**, 2423–2428 (2001).
48. G. Schaffar *et al*., Cellular toxicity of polyglutamine expansion proteins: Mechanism of transcription factor deactivation. *Mol. Cell* **15**, 95–105 (2004).
49. J. Linden, A. S. James, C. McDaniel, J. D. Jentsch, Dopamine D2 receptors in dopaminergic neurons modulate performance in a reversal learning task in mice. *eNeuro* **5**, ENEURO.0229-17.2018 (2018).
50. C. Zuccato, E. Cattaneo, Role of brain-derived neurotrophic factor in Huntington's disease. *Prog. Neurobiol.* **81**, 294–330 (2007).
51. F. Paraskevopoulou, M. A. Herman, C. Rosenmund, Glutamatergic innervation onto striatal neurons potentiates GABAergic synaptic output. *J. Neurosci.* **39**, 4448–4460 (2019).
52. N. Shahani *et al*., RasGRP1 promotes amphetamine-induced motor behavior through a Rhes interaction network ("Rhesactome") in the striatum. *Sci. Signal.* **9**, ra111 (2016).
53. Y. Kuo, S. Ren, U. Lao, B. A. Edgar, T. Wang, Suppression of polyglutamine protein toxicity by co-expression of a heat-shock protein 40 and a heat-shock protein 110. *Cell Death Dis.* **4**, e833–e11 (2013).
54. R. K. R. Kalathur *et al*., The unfolded protein response and its potential role in Huntington's disease elucidated by a systems biology approach. *F1000 Res.* **4**, 103 (2015).
55. R. G. Lim *et al*.; HD iPSC Consortium, Developmental alterations in Huntington's disease neural cells and pharmacological rescue in cells and mice. *Nat. Neurosci.* **20**, 648–660 (2017).
56. H. Jia *et al*., Histone deacetylase (HDAC) inhibitors targeting HDAC3 and HDAC1 ameliorate polyglutamine-elicited phenotypes in model systems of Huntington's disease. *Neurobiol. Dis.* **46**, 351–361 (2012).
57. H. Jia, C. D. Morris, R. M. Williams, J. F. Loring, E. A. Thomas, HDAC inhibition imparts beneficial transgenerational effects in Huntington's disease mice via altered DNA and histone methylation. *Proc. Natl. Acad. Sci. U.S.A.* **112**, E56–E64 (2015).
58. J. A. Girault, A. Costa, P. Derkinderen, J. M. Studler, M. Toutant, FAK and PYK2/CAKbeta in the nervous system: A link between neuronal activity, plasticity and survival? *Trends Neurosci.* **22**, 257–263 (1999).
59. J. A. Bartos *et al*., Postsynaptic clustering and activation of Pyk2 by PSD-95. *J. Neurosci.* **30**, 449–463 (2010).
60. M. Arancillo *et al*., Titration of syntaxin1 in mammalian synapses reveals multiple roles in vesicle docking, priming, and release probability. *J. Neurosci.* **33**, 16698–16714 (2013).
61. F. Paraskevopoulou, Impaired inhibitory GABAergic synaptic transmission and transcription studied in single neurons by Patch-seq in Huntington's disease. GEO. https://www.ncbi.nlm.nih.gov/geo/query/acc.cgi?acc=GSE171099. Deposited 29 March 2021.
62. O. Gokce *et al*., Cellular taxonomy of the mouse striatum as revealed by single-cell RNA-seq. *Cell Rep.* **16**, 1126–1137 (2016).